Structure
Short Article

Translation Initiation Factor eIF3b Contains a Nine-Bladed β-Propeller and Interacts with the 40S Ribosomal Subunit

Yi Liu,[1] Piotr Neumann,[1] Bernhard Kuhle,[1] Thomas Monecke,[1] Stephanie Schell,[2] Ashwin Chari,[2] and Ralf Ficner[1,*]
[1]Department of Molecular Structural Biology, Institute for Microbiology and Genetics, GZMB, Georg-August-University Göttingen, 37077 Göttingen, Germany
[2]Max-Planck-Institute for Biophysical Chemistry, 37077 Göttingen, Germany
*Correspondence: rficner@uni-goettingen.de
http://dx.doi.org/10.1016/j.str.2014.03.010

SUMMARY

The multisubunit eukaryotic translation initiation factor 3, among which the subunit b (eIF3b) is a major scaffold protein, plays essential roles in protein synthesis. Here, we report the crystal structure of the WD40 domain of *Chaetomium thermophilum* eIF3b, revealing a nine-bladed β-propeller fold. Sequence analysis indicates that this propeller architecture is common to all eIF3b orthologs. Revisiting the cryo-electron microscopy (cryo-EM) map of the 43S preinitiation complex suggests an interaction of the eIF3b with the 40S ribosomal subunit involving the ribosomal protein S9e and the 18S rRNA. This model is strongly supported by the direct binding of eIF3b to 40S ribosomes and to the isolated ribosomal protein rpS9e in vitro.

INTRODUCTION

In eukaryotes, the elongation-competent ribosome is assembled during the initiation phase on the mRNA start codon with the Met-tRNA$_i^{Met}$ in its P site. The fidelity of this critical step is ensured by a set of at least 12 different auxiliary protein factors, called eukaryotic translation initiation factors (eIFs) (Jackson et al., 2010). The largest among these factors is the multisubunit complex eIF3, which is involved in almost all steps of the initiation process (Hinnebusch, 2006). It associates with eIF1, eIF5, and the eIF2·GTP·Met-tRNA$_i^{Met}$ ternary complex and promotes their binding to the 40S ribosomal subunit during 43S preinitiation complex (PIC) assembly (Valášek et al., 2002, 2003). Moreover, eIF3 assists the subsequent recruitment of mRNA to the 43S PIC (Jivotovskaya et al., 2006; Korneeva et al., 2000) and mutation studies in yeast indicated an involvement of eIF3 in scanning and the stringent start codon selection (Chiu et al., 2010; Valášek et al., 2004).

In budding yeast, eIF3 is composed of five essential subunits (a/Tif32, b/Prt1, c/Nip1, i/Tif34, and g/Tif35), all of which have corresponding orthologs in the significantly larger eIF3 complex of other eukaryotes (13 subunits [a–m] in mammals), and the nonessential substoichiometric subunit Hcr1/eIF3j (Asano et al., 1998; Hinnebusch, 2006). Within the eIF3 complex, eIF3b plays a central role as scaffold protein that provides an interaction platform for the other core subunits. eIF3b is an ~90 kDa protein that has been predicted to fold into three independent domains (Marintchev and Wagner, 2004) (Figure 1A). The N-terminal domain (NTD) of eIF3b contains a structurally canonical RNA recognition motif (RRM) and is responsible for the binding to eIF3a and eIF3j (ElAntak et al., 2007; Valášek et al., 2001), while the eIF3b C-terminal domain (CTD) is necessary for the interaction with eIF3i and eIF3g (Asano et al., 1998; Herrmannová et al., 2012). The NTD and CTD are connected by the central WD40 domain, which was predicted to fold most likely into two seven-bladed β-propellers (Marintchev and Wagner, 2004). So far, structural information about eIF3b is limited to the N-terminal RRM domain (~100 amino acids) and an ~40 residue α helix of the CTD (ElAntak et al., 2007; Herrmannová et al., 2012; Khoshnevis et al., 2010). In contrast, neither functional nor structural information is available for the central WD40 repeats, which form ~65% of the protein and are highly conserved from yeast to humans.

The WD40 repeat is a small motif of ~40 amino acid residues usually forming a four-stranded antiparallel β sheet and often containing the eponymous Trp-Asp (WD) dipeptide at the C terminus (Xu and Min, 2011). Tandem WD40 repeats are radially arranged around a center axis, resulting in a multibladed, doughnut-like propeller architecture (Stirnimann et al., 2010). In most cases, the last blade of a propeller is composed of the N-terminal β strand situated in the outermost shell of the propeller and the last three C-terminal strands, creating a "$1_N + 3_C$ Velcro" closure that stabilizes the radial folding (Xu and Min, 2011). WD40 domains are involved in a wide range of cellular functions, commonly by serving as a rigid scaffold to facilitate protein-protein interactions (Stirnimann et al., 2010; Xu and Min, 2011). Consistent with their diversity in sequence length and composition, WD40 propellers vary considerably in their number of blades. To date, four- to ten-bladed WD40 β-propellers have been structurally identified, among which the seven-bladed propellers are the most abundant in the Protein Data Bank (PDB), followed by six and eight repeats (Chen et al., 2011).

Here, we report the crystal structure of the eIF3b WD40 β-propeller from *Chaetomium thermophilum* at 2.7 Å resolution, revealing an unforeseen nine-bladed propeller. Besides its nine-bladed architecture, the *ct*eIF3b WD40 propeller reveals several noncanonical folding properties. It uses an unusual "$3_N + 1_{C,innermost}$ Velcro" closure type and possesses a central

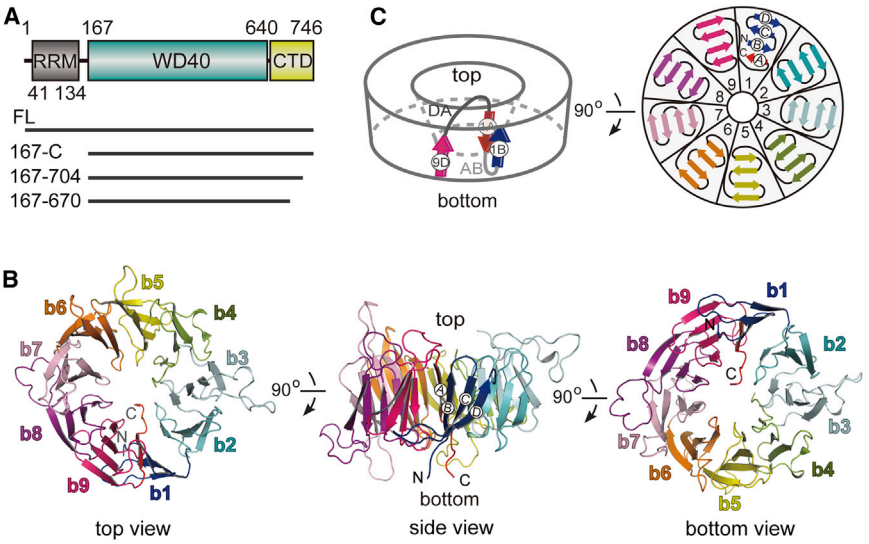

Figure 1. Overall Structure of *cte*IF3b-WD40

(A) Schematic domain organization of *cte*IF3b. The boundaries of the domains are indicated.

(B) Top, side, and bottom views of the overall structure of *cte*IF3b-WD40 in cartoon representation. Blades 1 to 9 are colored individually and N termini (N) as well as C termini (C) are labeled.

(C) Topology plot of the *cte*IF3b β-propeller fold. The left and right drawings are shown in orientations similar to the side and bottom views in (B), respectively.

See also Figure S1.

channel exhibiting the shape of a circular truncated cone rather than the common cylindrical form. On the basis of its unique shape, we were able to unambiguously fit the *cte*IF3b WD40 structure into the recently published cryo-EM map of the 43S PIC in a position previously assigned to the seven-bladed β-propeller protein eIF3i (Hashem et al., 2013). Because of this location in the shoulder region of the 40S ribosomal subunit, eIF3b is expected to be in close proximity to the ribosomal protein S9e. Consistently, we observed a stable interaction between eIF3b and the isolated protein rpS9e as well as with the 40S ribosomal subunit by in vitro binding studies. Hence, our data strongly argue for a direct involvement of eIF3b in the recruitment of eIF3 to the 40S ribosomal subunit and 43S PIC assembly.

RESULTS AND DISCUSSION

Overall Structure

Crystallization of full-length *cte*IF3b yielded crystals containing only the WD40 domain because of proteolytic cleavage during the crystallization process (Figure S1 available online). The crystal structure was solved de novo by means of multiwavelength anomalous dispersion (MAD) and refined at a resolution of 2.7 Å (Table 1). It comprises residues 165 to 638, with one region (loop residues 299 to 311) not defined in the electron density map.

Surprisingly, in contrast to the prediction of two tandem propellers (Marintchev and Wagner, 2004), the WD40 domain of *cte*IF3b actually adopts a single β-propeller fold composed of nine blades (Figure 1B). The nine blades are pseudosymmetrically arranged in sequential order around a central channel. Each blade of the propeller is formed by a β sheet consisting of four antiparallel strands, designated A, B, C, and D from the inside to the outside of the propeller. Different from the common "$1_N + 3_C$ Velcro" closure of the β-propeller fold (Xu and Min, 2011), the WD40 repeats of *cte*IF3b apply a "$3_N + 1_C$" arrangement whereby the last C-terminal β strand is positioned as the innermost strand of the first blade (Figures 1B and 1C). Another unusual feature of the nine-bladed *cte*IF3b WD40 propeller is that the central channel resembles a circular truncated cone (Figures 1B and 1C). The diameter of the channel on the "bottom" side is ~22.4 Å, which is further decreased to ~15.6 Å by the conserved AB loops, compared with the increased average diameter of 29.5 Å at the "top." The outermost shape of the *cte*IF3b propeller is almost cylindrical, as revealed by the overall diameters of 51.5 Å and 53.6 Å for the bottom and top parts of the propeller, respectively. When compared with seven- and eight-bladed propellers, the additional blade(s) of the *cte*IF3b WD40 expand the propeller's dimensions, volume, and accessible surface area. Taken together, this might be of functional relevance for eIF3b's role as a central scaffold protein within eIF3 and its simultaneous association with proteins and rRNA of the 40S ribosomal subunit (see below).

Sequence and Structural Conservation of eIF3b

Structure-based sequence alignments of the WD40 repeats of *cte*IF3b reveal several conserved sequence characteristics, notably the Trp-X-Pro (where X represents any amino acid) motif at the end of strands A and the Phe/Tyr-Φ (where Φ stands for a hydrophobic amino acid) segment in strands B, as well as hydrophobic residues in strands D (Figure 2A). However, the Trp-Asp (WD) dipeptide located at the ends of strands C is present only in blades 3 and 8. The Trp residue of the WD motif has been replaced by the aromatic amino acid Tyr (in blades 4 and 9), Phe (in blades 6 and 7), and the hydrophobic Met in blade 5, whereas the Asp has been substituted by other polar residues, with the only exception of a Gly in blade 2 (Figure 2A). The repeating motifs (single blades) within the *cte*IF3b WD40 domain are structurally well conserved, with a root-mean-square deviation (rmsd) ranging from 0.94 Å to 1.57 Å for all Cα atoms, whose positions differed less than 3 Å, when superimposing each blade onto blade 1 (Figure 2B).

A multiple-sequence alignment reveals that eIF3b orthologs from different organisms vary considerably in the NTD but are well conserved in the WD40 domain as well as in the C-terminal part of the protein (Figure S2). Secondary structure predictions (using the PSIPRED server; Buchan et al., 2013) of eIF3b orthologs assign 35 or 36 β strands to their WD40 domains, indicating that the nine-bladed WD40 β-propeller fold of *cte*IF3b is not a unique instance but is used universally by eIF3b orthologs. Many of the identical residues among the orthologs are hydrophobic and located in the structural core of the WD propeller (Figure S2), indicating their role in accurate folding and stability. Additionally, two

Table 1. Data Collection and Structure Refinement Statistics

	Se-Met Derivative, MAD			
	Peak	Inflection	Remote	Native
Data Collection				
Wavelength (Å)	0.9798	0.9799	0.9775	0.8266
Space group	$P4_32_12$	$P4_32_12$	$P4_32_12$	$P4_32_12$
Resolution (Å)	50–3.25 (3.35–3.25)	50–3.30 (3.40–3.30)	50–3.31 (3.41–3.31)	50–2.72 (2.82–2.72)
Cell dimensions				
a (Å)	108.32	108.31	108.28	108.38
b (Å)	108.32	108.31	108.28	108.38
c (Å)	186.88	186.90	186.84	172.18
Unique reflections	32,904 (2,863)	31,367 (2,719)	30,923 (2,659)	28,259 (2,828)
Redundancy	3.1 (2.9)	3.1 (3.0)	2.7 (2.7)	8.5 (8.6)
Completeness (%)	98.2 (98.9)	98.0 (98.7)	97.9 (98.6)	99.9 (100.0)
R_{merge} (%)	9.2 (73.8)	9.0 (61.0)	9.5 (60.3)	5.7 (61.5)
I/σ (I)	11.67 (1.76)	12.45 (2.13)	10.71 (1.90)	25.67 (3.48)
$CC_{1/2}$	99.7 (66.5)	99.7 (74.5)	99.5 (67.7)	99.9 (92.0)
Phasing				
Anomalous correlation[a]	47 (4)	34 (11)	28 (12)	
SigAno[a]	1.33 (0.78)	1.16 (0.83)	1.08 (0.82)	
FOM after *DM*	0.573			
Structure Refinement				
Resolution range (Å)				48.47–2.72 (2.82–2.72)
Completeness (%)				100.0 (100.0)
R_{work}/R_{free} (%)[b]				20.56/22.98
No. of atoms				
Total				3,819
Protein				3,764
Solvent				51
Ions				4
Rmsd bonds (Å)				0.003
Rmsd angles (°)				0.806
B factor (Å^2)				
Average				74.8
Protein				75.0
Solvent				61.8
Ions				97.0
Wilson B factor (Å^2)[c]				66.87
Solvent content (%)				73
Ramachandran plot				
Favored (%)				95.19
Allowed (%)				4.81
Outliers (%)				0.0

Values for the data in the highest resolution shell are shown in parentheses.
[a]Anomalous correlation and mean anomalous difference (SigAno), calculated with *XSCALE*.
[b]$R_{free} = \sum_{Test}||F_{obs}| - |F_{calc}||/\sum_{Test}|F_{obs}|$, where "Test" is a test set of about 5% of the total reflections randomly chosen and set aside before refinement for the complex.
[c]Wilson B factor was estimated with phenix.refine package.

clusters of surface residues are highly conserved from yeast to humans (Figure 2C), suggesting a potential role in binding other proteins and/or the other eIF3b domains. The first conserved surface region is located on the side of the propeller and consists of residues mainly belonging to blades 5 and 6; the second conserved area is situated primarily on the top of the propeller, involving residues from the AB loops of blades 9, 1, 2, and 3 and the D strands of blades 1 and 2 (Figure 2C). Interestingly, both

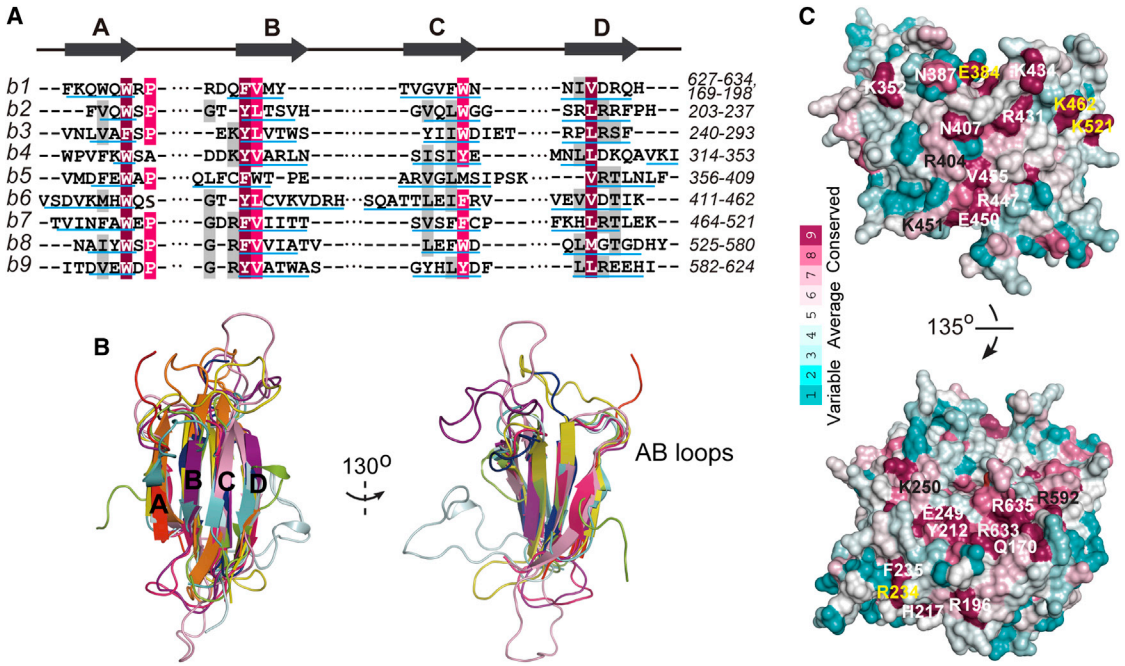

Figure 2. Sequence and Structural Conservation of eIF3b

(A) Sequence alignment of the nine β sheets of *cte*IF3b-WD40. Residues are colored according to the conservation pattern (highly conserved: dark red; conserved: pink). Residues forming the β strands are underlined, and arrows on the top indicate the positions of strands A to D.

(B) Superposition of the nine β-propeller blades of *cte*IF3b. The blades are colored as in Figure 1B. In the image on the right, the long β sheet 6 was omitted for clarity reasons.

(C) Surface representation of *cte*IF3b-WD40 with sequence conservation represented in the color-coding bar, ranging from cyan (variable) to purple (conserved). The conservation scores were generated by ConSurf (http://consurf.tau.ac.il) using the sequence alignment of eIF3b-WD40 as shown in Figure S2. Highly conserved surface residues are labeled.

conserved surface areas of *cte*IF3b-WD40 mainly contain hydrophobic and positively charged residues, which could be involved in RNA binding (Figure S3).

To address the question of whether the nine-bladed WD40 β-propeller fold can also be found in proteins other than eIF3b orthologs, we searched the National Center for Biotechnology Information Conserved Domain Database (Marchler-Bauer et al., 2011). We identified eIF2A, an alternative initiator tRNA-binding protein involved in internal ribosome entry site-mediated translation initiation (Reineke et al., 2011), as a potential candidate, even though the sequence identity between the WD40 domains of eIF2A and eIF3b is only 20%. The secondary structure prediction of eIF2A assigns 36 β strands, exactly matching the strands number of a nine-bladed β-propeller. While this manuscript was under revision, the crystal structure of eIF2A became available (PDB accession number 3WJ9; Kashiwagi et al., 2014), revealing an almost identical nine-bladed β-propeller fold, which is reflected by an rmsd of 1.79 Å for 300 common Cα atoms of the eIF2A and eIF3b structures. However, the high degree of sequence degeneracy among WD40 domains makes the prediction of the correct blade number and domain boundaries and therefore of other nine-bladed β-propeller very difficult.

eIF3b Serves as the Central Scaffold Subunit for the eIF3 Core Complex in *C. thermophilum*

The genome of *C. thermophilum* contains 13 genes encoding eIF3 subunits, suggesting that *cte*IF3 resembles mammalian eIF3. Like its yeast counterpart, *cte*IF3 contains a stable five-subunit core, as shown by means of analytical size-exclusion chromatography (SEC) (Figure 3A). The conservation between yeast and *C. thermophilum* is also reflected by the existence of two distinct subcomplexes containing eIF3b, which consist of eIF3a,b,c and eIF3b,g,i respectively (Figures 3B and 3C). However, in contrast to yeast eIF3 (Khoshnevis et al., 2012), a stable eIF3b-c-i-g subcomplex could not be reconstituted in vitro from *C. thermophilum* proteins (Figure S4). This indicates that the interaction between eIF3c and the eIF3b-i-g subcomplex is either not universal and therefore might not be essential for the assembly of the eIF3 complex or depends on the presence of additional subunits of eIF3 in *C. thermophilum*.

Localization of eIF3b on the 40S Ribosomal Subunit

It has previously been demonstrated by both biochemical studies and cryo-EM reconstructions that eIF3 associates with the solvent-exposed side of the 40S ribosomal subunit. Biochemical investigations suggested that the eIF3 core is located in the head and shoulder regions of the 40S, while the cryo-EM structures indicated that the major part of eIF3 is anchored underneath the platform of the 40S (Hashem et al., 2013; Siridechadilok et al., 2005; Valášek, 2012). In the cryo-EM map of the rabbit 43S PIC bound to helicase DHX29 (Electron Microscopy Data Bank [EMDB] accession number 5658), the seven-bladed β-propeller protein eIF3i was fitted into a doughnut-like density below the shoulder of the 40S subunit;

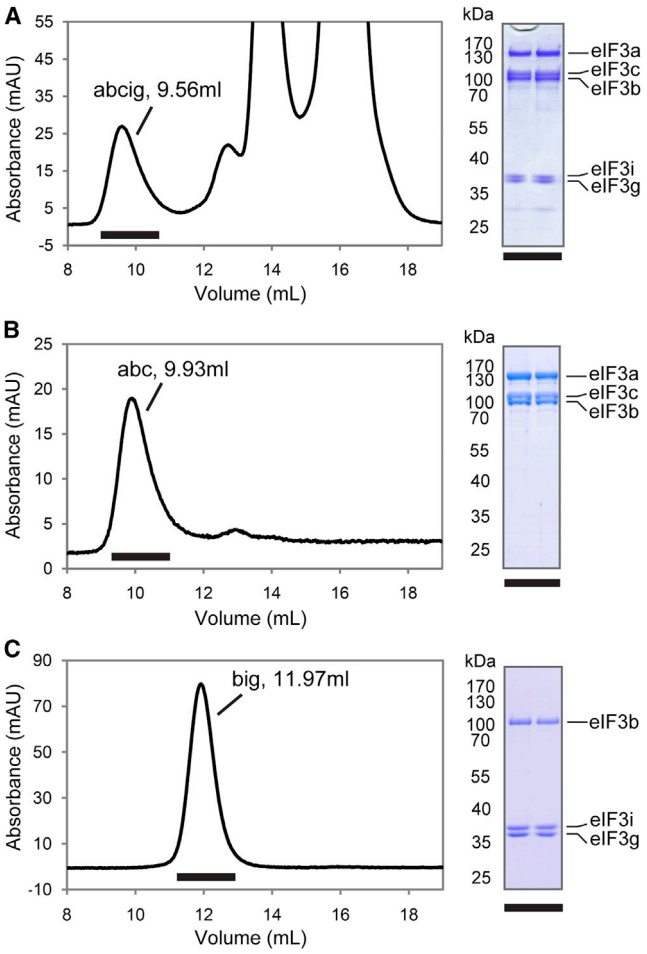

Figure 3. Analytical SEC of *cte*IF3 Subcomplexes

Analytical SEC profiles of the five-component *cte*IF3 core (A), the *cte*IF3a-b-c subcomplex (B), and the *cte*IF3b-i-g subcomplex (C), respectively. The corresponding SDS-PAGE gels are shown in the right panel.

however, the possibility that this density originated from the β-propeller of eIF3b could not be excluded (Figure 4A) (Hashem et al., 2013). Notably, this cryo-EM segment definitely possesses a channel with a wide top and narrow bottom. As aforementioned, the WD40 domain of eIF3b harbors a channel with similar geometric parameters, which reaches a consensus with the cryo-EM density on the axle outline (Figures 1B, 4B, and 4C). By contrast, eIF3i holds a channel that has a similar width on both sides (PDB accession number 3ZWL). Additionally, the overall size of eIF3i is too small to fully explain this segmented EM density (Figure S5). Because of the lack of technical details, we could not repeat the fitting of eIF3i to the doughnut-like density and reach a similar result as reported (Hashem et al., 2013). Our fit of eIF3i using UCSF Chimera 1.8 (Pettersen et al., 2004) resulted in a cross-correlation coefficient (CCC) of 0.52 and 38.5% atom outliers. The fitting statistics significantly improved when the WD40 propeller (without the nonconserved loops) of *cte*IF3b was positioned in the doughnut-like density (Figure S5), with a corresponding CCC of 0.91 and only 17% of the atoms outside the density. On the basis of our fit, the surface formed by highly conserved residues of blades 5 and 6 of the propeller is oriented toward the ribosomal protein S9e (rpS9e) and the rRNA helix h16 (Figures 4B and 4C). The EM density also indicates a possible interaction between the rRNA expansion segment ES6^{S}-hA and blade 9 and/or conserved basic residues C-terminally adjacent to the WD40 domain (Figure 4D; Figure S2).

The position of eIF3b directly below the shoulder of the 40S is in good agreement with previous studies, as eIF3j, which interacts with eIF3b-RRM via its NTD, has been proposed to bind to the 40S mRNA entry channel adjacent to the shoulder of the 40S subunit (ElAntak et al., 2007; Elantak et al., 2010; Fraser et al., 2007; Nielsen et al., 2006).

Interaction between eIF3b and the 40S Ribosomal Subunit

The interpretation of the EM map described above suggests a direct interaction of eIF3b with the 40S ribosomal subunit. Thus far, no biochemical evidence exists for such an interaction, and therefore we sought a biochemical validation. For this, purified *C. thermophilum* 40S ribosomal subunits were incubated with increasing amounts of *cte*IF3b and their mutual interaction studied by cosedimentation experiments. Upon the addition of *cte*IF3b, we noted the appearance of an additional ~86 kDa protein in the pellet, which is absent in purified *ct*40S subunits, indicating a stable association. Under these experimental conditions, unbound eIF3b remained in the supernatant (Figure 4E). In addition, *cte*IF3b$^{167\text{-}670}$ (containing the WD40 domain plus an ~30-residue C-terminal extension) also binds to the *ct*40S subunit (Figure S6A), suggesting that the N-terminal RRM domain is dispensable for binding.

Our interpretation of the 43S PIC EM 3D reconstruction places eIF3b next to the ribosomal protein rpS9e, which could be verified by pull-down assays. Both full-length *cte*IF3b and N-terminally truncated *cte*IF3b$^{167\text{-}C}$ bind to glutathione S-transferase (GST)-tagged *ctr*pS9e (Figure 4F), while *cte*IF3b$^{167–670}$ and *cte*IF3b$^{167–704}$ fail to do so (Figure S6B). This implies that the 42 C-terminal residues of *cte*IF3b are crucial for the interaction with *ctr*pS9e. Importantly, the interaction of *cte*IF3b-CTD is not a prerequisite for binding to the *ct*40S ribosomal subunit, as *cte*IF3b$^{167–670}$ is still capable of this association (Figure S6A). Thus, interactions with other parts of the *ct*40S ribosome (e.g., the rRNA ES6^{S}-hA) are sufficient for stable association.

Because the eIF3b-CTD also contains binding sites for eIF3i and eIF3g, we further tested whether the interaction between *cte*IF3b and *ctr*pS9e affects the binding of *cte*IF3i and *cte*IF3g to *cte*IF3b. The observed quaternary complex (Figure 4F) suggests that these intermolecular interactions are not mutually exclusive. Consistently, the rpS9e binding site of eIF3b is located C-terminally to the α helix, which interacts with the eIF3i β-propeller (Herrmannová et al., 2012). Interestingly, the NTD of *cte*IF3b apparently also contributes to the formation of the *ctr*pS9e-eIF3b,g,i complex, as the N-terminally truncated *cte*IF3b$^{167\text{-}C}$ exhibits a lower affinity to eIF3g,i (Figure 4F).

With regard to the 43S PIC/DHX29 EM map, we expect the C-terminal 42 residues of eIF3b to fill some of the noninterpreted density between rpS9e and the β-propeller. There is also some unassigned density protruding from the β-propeller (Figure 4B). Because this density is adjacent to both the N and C termini of

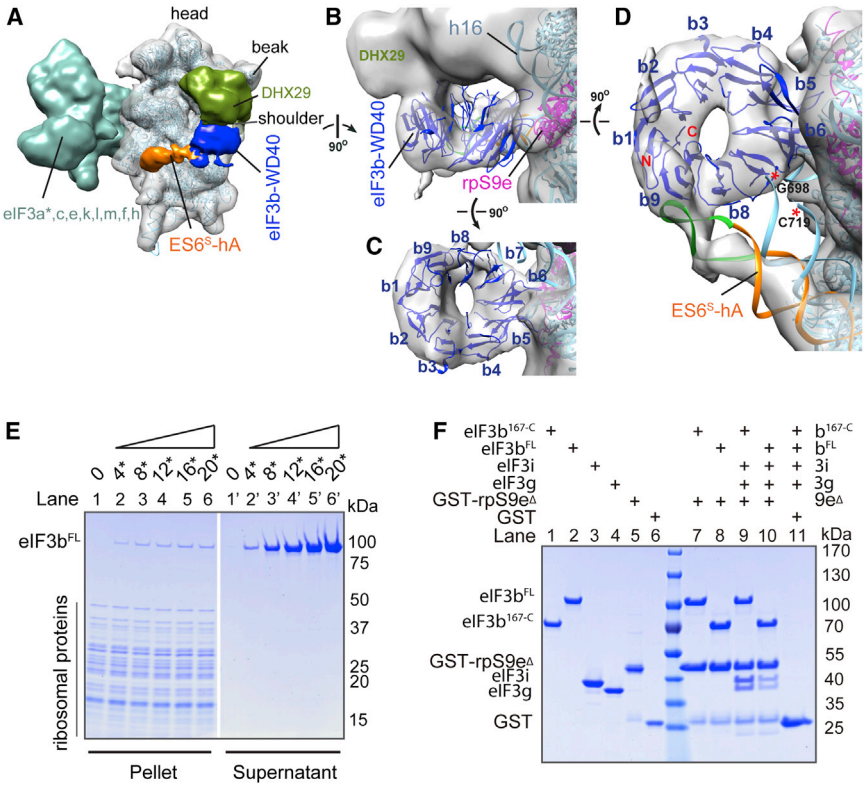

Figure 4. Interaction of eIF3b with the 40S Ribosomal Subunit

(A–D) Localization of eIF3b on the 40S ribosome. The nonconserved loop insertions of *ct*eIF3b-WD40, which are absent in rabbit eIF3b, were removed before fitting. In (C) and (D), the density assigned to DHX29 was removed for clarity.

(A) Overall view of the position of eIF3b-WD40 β-propeller on the 40S ribosomal subunit (EMDB accession number 5658). eIF3b-WD40 (blue) is located below the shoulder of the 40S and is disconnected from the eIF3 subcomplex containing the subunits a*, c, e, f, h, k, l, and m (cyan). The asterisk marks a truncated version of eIF3a.

(B) Detail side view of eIF3b-WD40 localization. The rpS9e and the rRNA helix h16 are indicated.

(C) Top view of eIF3b-WD40 showing the characteristic conical central channel.

(D) Structural model of a possible interaction between the eIF3b WD40 propeller and the 18S rRNA expansion segment $ES6^S$-hA. The rRNA helix was manually fitted into the EM density portion using the crystal structure of the 40S ribosome (PDB accession number 4KZZ; Lomakin and Steitz, 2013). Nineteen nucleotides of $ES6^S$-hA, which are missing in the crystal structure, have been modeled (colored green) to illustrate their potential extension.

(E) Binding of *ct*eIF3b to *ct*40S ribosomes. Incubation of increasing amounts of *ct*eIF3b leads to the cosedimentation with *ct*40S subunits (lanes 2–6), while excess *ct*eIF3b remains in the supernatant (lanes 2′–6′). Lanes 1 and 1′ represent *ct*40S in the absence of *ct*eIF3b.

(F) Interaction of *ct*eIF3b and *ct*rpS9e by GST pull-down assay. Lanes 1 to 6 show the isolated proteins as a reference. Lanes 7 to 11 show the elution fractions of the GST pull-down after the removal of unbound proteins and extensive washing. $rpS9e^{\Delta}$ corresponds to *ct*$rpS9e^{1–183}$.

the β-propeller (Figure 4D), it could either correspond to one of the α helices predicted between the β-propeller and the C-terminal 42 residues or belong to the linker connecting the eIF3b NTD. However, an unambiguous localization of the missing NTD and CTD is currently not feasible and would be highly speculative.

Structure of eIF3

In the EM structure of the 43S PIC/DHX29 complex, the position of the eIF3b WD40 domain appears to be rather distant to the complex of the eight eIF3 subunits a*, c, e, f, h, k, l, and m (Figure 4A). However, the structure of this octameric complex mainly represents a core formed by the PCI/MPN domains (proteasome, COP9, initiation factor 3/Mpr1, Pad1 N-terminal), whereas other domains of these subunits are not defined in the EM map. This is consistent with previous EM structures of full eIF3, which have unraveled the structure of the octameric PCI/MPN complex. However, other domains and the subunits b, d, g, and i are also missing in these EM structures, most likely because of the high flexibility and dynamics of isolated eIF3 (Querol-Audi et al., 2013; Sun et al., 2011). Furthermore, in the 43S PIC/DHX29 complex, eIF3a is lacking some 600 C-terminal residues and is therefore denoted as a*. Thus, the missing and flexible parts of eIF3 subunits would be sufficient to fill the gap between the PCI/MPN core and the eIF3b WD40 domain.

In summary, our studies support a direct binding of eIF3b to the 40S ribosomal subunit, which suggests an essential role of the central scaffold subunit eIF3b in the formation of the 43S PIC and might provide a structural basis for dissecting the mechanisms of the assembly of 43S and 48S PIC.

EXPERIMENTAL PROCEDURES

Cloning, Expression, Protein Purification, and Crystallization

C. thermophilum eIF3a, b, c, i, g, and rpS9e genes were amplified from genomic DNA or cDNA and cloned into the pGEX-6P-1 (GE Healthcare) or pET28b (Merck) vector for expression in *Escherichia coli* cells. Proteins were purified using GST-affinity or immobilized metal affinity chromatography, ion exchange, and gel filtration chromatography. Both native and selenomethionine (Se-Met) derivative crystals were obtained at 20°C using the sitting drop vapor diffusion method with reservoir solution containing 15% polyethylene glycol 20k, 0.08 M $MnCl_2$, and 0.1 M MES buffer (pH 6.5). Details regarding the cloning, expression, purification, and crystallization are described in Supplemental Experimental Procedures.

X-Ray Data Processing and Structure Determination

X-ray diffraction data of a native and a Se-Met *ct*eIF3b crystal were processed and scaled using XDS (Kabsch, 2010) up to resolutions of 2.72 Å and 3.30 Å, respectively (Table 1). Crystals belong to space group $P4_32_12$. The Matthews coefficient (4.6 $Å^3$/Da) suggested the presence of one protein molecule in the asymmetric unit corresponding to a solvent content of 73%. The crystal structure was solved by means of three-wavelength Se-Met MAD combined with automatic model building. Final refinement was performed with PHENIX (Adams et al., 2010). Figures showing crystal structures were made with PyMOL (http://www.pymol.org) or UCSF Chimera 1.8 (Pettersen et al., 2004). Details are described in Supplemental Experimental Procedures.

Fitting of eIF3b-WD40 into the EM Map

Fitting of the eIF3b crystal structure into the cryo-EM map of the 43S PIC+ DHX29 from rabbit (EMDB accession number 5658) was done using UCSF Chimera 1.8 (Pettersen et al., 2004). The voxel size and contour level were set to 2.245 Å and 0.019 on the object scale, respectively. Nonconserved loops, which are present in *ct*eIF3b-WD40 but not in the rabbit eIF3b, were removed prior to fitting. *ct*eIF3b-WD40 was fitted in a local six-dimensional search as a rigid-body into the doughnut-like EM density portion using the fit to map algorithm as implemented in Chimera. A CCC defining the agreement of a simulated map of the crystal structure (resolution 10 Å) and the EM map as well as the respective number of outlier atoms relative to all atoms were calculated, and the fit with highest CCC was accepted. In order to validate the model further, fitting was repeated using the program package Sculptor 2.1.1_r1 (Birmanns et al., 2011), obtaining virtually identical results.

Purification of *C. thermophilum* 40S Ribosomal Subunit and Interaction Studies with *ct*eIF3b

C. thermophilum cultivation and purification of 80S ribosomes were performed as described (Amlacher et al., 2011; Leidig et al., 2013). *ct*80S ribosomes were dissociated into subunits using puromycin and separated on a sucrose density gradient (Blobel and Sabatini, 1971). Fractions containing pure *ct*40S ribosomes were pooled. Interaction with $eIF3b^{FL}$ or $eIF3b^{167–670}$ (using 4, 8, 12, 16, 20, or 5, 15-fold molar excess) were tested by sedimentation through 30% sucrose cushions in an MLA-130 rotor (Beckman) run at 100,000 rpm for 2 hr at 4°C. Supernatants were carefully decanted, and the pellets were resuspended. Both sucrose cushions and resuspension buffers were in 50 mM BisTris (pH 6.8), 50 mM KCl, 10 mM $MgCl_2$, and 5 mM dithiothreitol.

GST Pull-Down Assays

Fifty micrograms of GST fusion protein was immobilized on glutathione Sepharose (GE Healthcare Life Sciences) beads and subsequently mixed with a 2-fold molar excess of the nontagged protein. After 30 min of incubation and extensive washing, the proteins were eluted and analyzed by SDS-PAGE (for details, see Supplemental Experimental Procedures).

ACCESSION NUMBERS

Atomic coordinates and structure factors have been deposited in the PDB (accession number 4NOX).

SUPPLEMENTAL INFORMATION

Supplemental Information includes Supplemental Experimental Procedures and six figures and can be found with this article online at http://dx.doi.org/10.1016/j.str.2014.03.010.

AUTHOR CONTRIBUTIONS

Y.L., B.K., and R.F. designed the experiments. Y.L. performed the protein expression, purification, and crystallization of *ct*eIF3b. Y.L. and P.N. performed crystal structure analysis. Y.L., S.S., and A.C. prepared 40S ribosomes and performed sedimentation studies. Y.L. performed interaction studies with rpS9e. Y.L. and B.K. performed the in vitro reconstitution of *ct*eIF3 subcomplexes. Y.L. and T.M. performed the interpretation of the EM map. Y.L., B.K., T.M., P.N., S.S., A.C., and R.F. wrote the manuscript.

ACKNOWLEDGMENTS

We thank the staff of the beamlines P13 (PETRA III, Deutsches Elektronen-Synchrotron) and BL14.1 at BESSY-II (Helmholtz-Zentrum Berlin für Materialien und Energie) electron storage ring (Berlin, Germany) for support during X-ray diffraction data collection. This work was supported by a grant from the Deutsche Forschungsgemeinschaft to A.C. (CH1098/1-1). We are grateful to Achim Dickmanns for critically reading this manuscript and for helpful discussions.

Received: December 10, 2013
Revised: March 13, 2014
Accepted: March 21, 2014
Published: April 24, 2014

REFERENCES

Adams, P.D., Afonine, P.V., Bunkóczi, G., Chen, V.B., Davis, I.W., Echols, N., Headd, J.J., Hung, L.W., Kapral, G.J., Grosse-Kunstleve, R.W., et al. (2010). PHENIX: a comprehensive Python-based system for macromolecular structure solution. Acta Crystallogr. D Biol. Crystallogr. *66*, 213–221.

Amlacher, S., Sarges, P., Flemming, D., van Noort, V., Kunze, R., Devos, D.P., Arumugam, M., Bork, P., and Hurt, E. (2011). Insight into structure and assembly of the nuclear pore complex by utilizing the genome of a eukaryotic thermophile. Cell *146*, 277–289.

Asano, K., Phan, L., Anderson, J., and Hinnebusch, A.G. (1998). Complex formation by all five homologues of mammalian translation initiation factor 3 subunits from yeast Saccharomyces cerevisiae. J. Biol. Chem. *273*, 18573–18585.

Birmanns, S., Rusu, M., and Wriggers, W. (2011). Using Sculptor and Situs for simultaneous assembly of atomic components into low-resolution shapes. J. Struct. Biol. *173*, 428–435.

Blobel, G., and Sabatini, D. (1971). Dissociation of mammalian polyribosomes into subunits by puromycin. Proc. Natl. Acad. Sci. USA *68*, 390–394.

Buchan, D.W., Minneci, F., Nugent, T.C., Bryson, K., and Jones, D.T. (2013). Scalable web services for the PSIPRED Protein Analysis Workbench. Nucleic Acids Res. *41* (Web Server issue), W349–W357.

Chen, C.K., Chan, N.L., and Wang, A.H. (2011). The many blades of the β-propeller proteins: conserved but versatile. Trends Biochem. Sci. *36*, 553–561.

Chiu, W.L., Wagner, S., Herrmannová, A., Burela, L., Zhang, F., Saini, A.K., Valásek, L., and Hinnebusch, A.G. (2010). The C-terminal region of eukaryotic translation initiation factor 3a (eIF3a) promotes mRNA recruitment, scanning, and, together with eIF3j and the eIF3b RNA recognition motif, selection of AUG start codons. Mol. Cell. Biol. *30*, 4415–4434.

ElAntak, L., Tzakos, A.G., Locker, N., and Lukavsky, P.J. (2007). Structure of eIF3b RNA recognition motif and its interaction with eIF3j: structural insights into the recruitment of eIF3b to the 40 S ribosomal subunit. J. Biol. Chem. *282*, 8165–8174.

Elantak, L., Wagner, S., Herrmannová, A., Karásková, M., Rutkai, E., Lukavsky, P.J., and Valásek, L. (2010). The indispensable N-terminal half of eIF3j/HCR1 cooperates with its structurally conserved binding partner eIF3b/PRT1-RRM and with eIF1A in stringent AUG selection. J. Mol. Biol. *396*, 1097–1116.

Fraser, C.S., Berry, K.E., Hershey, J.W., and Doudna, J.A. (2007). eIF3j is located in the decoding center of the human 40S ribosomal subunit. Mol. Cell *26*, 811–819.

Hashem, Y., des Georges, A., Dhote, V., Langlois, R., Liao, H.Y., Grassucci, R.A., Hellen, C.U., Pestova, T.V., and Frank, J. (2013). Structure of the mammalian ribosomal 43S preinitiation complex bound to the scanning factor DHX29. Cell *153*, 1108–1119.

Herrmannová, A., Daujotyte, D., Yang, J.C., Cuchalová, L., Gorrec, F., Wagner, S., Dányi, I., Lukavsky, P.J., and Valásek, L.S. (2012). Structural analysis of an eIF3 subcomplex reveals conserved interactions required for a stable and proper translation pre-initiation complex assembly. Nucleic Acids Res. *40*, 2294–2311.

Hinnebusch, A.G. (2006). eIF3: a versatile scaffold for translation initiation complexes. Trends Biochem. Sci. *31*, 553–562.

Jackson, R.J., Hellen, C.U., and Pestova, T.V. (2010). The mechanism of eukaryotic translation initiation and principles of its regulation. Nat. Rev. Mol. Cell Biol. *11*, 113–127.

Jivotovskaya, A.V., Valásek, L., Hinnebusch, A.G., and Nielsen, K.H. (2006). Eukaryotic translation initiation factor 3 (eIF3) and eIF2 can promote mRNA binding to 40S subunits independently of eIF4G in yeast. Mol. Cell. Biol. *26*, 1355–1372.

Kabsch, W. (2010). XDS. Acta Crystallogr. D Biol. Crystallogr. *66*, 125–132.

Kashiwagi, K., Ito, T., and Yokoyama, S. (2014). Crystal structure of the eukaryotic translation initiation factor 2A from Schizosaccharomyces pombe. J. Struct. Funct. Genomics. Published online February 26, 2014. http://dx.doi.org/10.1007/s10969-014-9177-y.

Khoshnevis, S., Neumann, P., and Ficner, R. (2010). Crystal structure of the RNA recognition motif of yeast translation initiation factor eIF3b reveals differences to human eIF3b. PLoS ONE *5*, e12784.

Khoshnevis, S., Hauer, F., Milón, P., Stark, H., and Ficner, R. (2012). Novel insights into the architecture and protein interaction network of yeast eIF3. RNA *18*, 2306–2319.

Korneeva, N.L., Lamphear, B.J., Hennigan, F.L., and Rhoads, R.E. (2000). Mutually cooperative binding of eukaryotic translation initiation factor (eIF) 3 and eIF4A to human eIF4G-1. J. Biol. Chem. *275*, 41369–41376.

Leidig, C., Bange, G., Kopp, J., Amlacher, S., Aravind, A., Wickles, S., Witte, G., Hurt, E., Beckmann, R., and Sinning, I. (2013). Structural characterization of a eukaryotic chaperone—the ribosome-associated complex. Nat. Struct. Mol. Biol. *20*, 23–28.

Lomakin, I.B., and Steitz, T.A. (2013). The initiation of mammalian protein synthesis and mRNA scanning mechanism. Nature *500*, 307–311.

Marchler-Bauer, A., Lu, S., Anderson, J.B., Chitsaz, F., Derbyshire, M.K., DeWeese-Scott, C., Fong, J.H., Geer, L.Y., Geer, R.C., Gonzales, N.R., et al. (2011). CDD: a Conserved Domain Database for the functional annotation of proteins. Nucleic Acids Res. *39* (Database issue), D225–D229.

Marintchev, A., and Wagner, G. (2004). Translation initiation: structures, mechanisms and evolution. Q. Rev. Biophys. *37*, 197–284.

Nielsen, K.H., Valásek, L., Sykes, C., Jivotovskaya, A., and Hinnebusch, A.G. (2006). Interaction of the RNP1 motif in PRT1 with HCR1 promotes 40S binding of eukaryotic initiation factor 3 in yeast. Mol. Cell. Biol. *26*, 2984–2998.

Pettersen, E.F., Goddard, T.D., Huang, C.C., Couch, G.S., Greenblatt, D.M., Meng, E.C., and Ferrin, T.E. (2004). UCSF Chimera—a visualization system for exploratory research and analysis. J. Comput. Chem. *25*, 1605–1612.

Querol-Audi, J., Sun, C., Vogan, J.M., Smith, M.D., Gu, Y., Cate, J.H., and Nogales, E. (2013). Architecture of human translation initiation factor 3. Structure *21*, 920–928.

Reineke, L.C., Cao, Y., Baus, D., Hossain, N.M., and Merrick, W.C. (2011). Insights into the role of yeast eIF2A in IRES-mediated translation. PLoS ONE *6*, e24492.

Siridechadilok, B., Fraser, C.S., Hall, R.J., Doudna, J.A., and Nogales, E. (2005). Structural roles for human translation factor eIF3 in initiation of protein synthesis. Science *310*, 1513–1515.

Stirnimann, C.U., Petsalaki, E., Russell, R.B., and Müller, C.W. (2010). WD40 proteins propel cellular networks. Trends Biochem. Sci. *35*, 565–574.

Sun, C., Todorovic, A., Querol-Audí, J., Bai, Y., Villa, N., Snyder, M., Ashchyan, J., Lewis, C.S., Hartland, A., Gradia, S., et al. (2011). Functional reconstitution of human eukaryotic translation initiation factor 3 (eIF3). Proc. Natl. Acad. Sci. USA *108*, 20473–20478.

Valásek, L.S. (2012). 'Ribozoomin'—translation initiation from the perspective of the ribosome-bound eukaryotic initiation factors (eIFs). Curr. Protein Pept. Sci. *13*, 305–330.

Valásek, L., Phan, L., Schoenfeld, L.W., Valásková, V., and Hinnebusch, A.G. (2001). Related eIF3 subunits TIF32 and HCR1 interact with an RNA recognition motif in PRT1 required for eIF3 integrity and ribosome binding. EMBO J. *20*, 891–904.

Valásek, L., Nielsen, K.H., and Hinnebusch, A.G. (2002). Direct eIF2-eIF3 contact in the multifactor complex is important for translation initiation in vivo. EMBO J. *21*, 5886–5898.

Valásek, L., Mathew, A.A., Shin, B.S., Nielsen, K.H., Szamecz, B., and Hinnebusch, A.G. (2003). The yeast eIF3 subunits TIF32/a, NIP1/c, and eIF5 make critical connections with the 40S ribosome in vivo. Genes Dev. *17*, 786–799.

Valásek, L., Nielsen, K.H., Zhang, F., Fekete, C.A., and Hinnebusch, A.G. (2004). Interactions of eukaryotic translation initiation factor 3 (eIF3) subunit NIP1/c with eIF1 and eIF5 promote preinitiation complex assembly and regulate start codon selection. Mol. Cell. Biol. *24*, 9437–9455.

Xu, C., and Min, J. (2011). Structure and function of WD40 domain proteins. Protein Cell *2*, 202–214.

Structure, Volume *22*

Supplemental Information

Translation Initiation Factor eIF3b Contains a Nine-Bladed β-Propeller and Interacts with the 40S Ribosomal Subunit

Yi Liu, Piotr Neumann, Bernhard Kuhle, Thomas Monecke, Stephanie Schell, Ashwin Chari, and Ralf Ficner

Supplemental Information

Translation initiation factor eIF3b contains a nine-bladed β-propeller and interacts with the 40S ribosomal subunit

Yi Liu, Piotr Neumann, Bernhard Kuhle, Thomas Monecke, Stephanie Schell, Ashwin Chari, Ralf Ficner

Inventory of Supplemental Information

Supplemental Data

Figure S1, related to Figure 1, showing the SDS-PAGE of full-length *ct*eIF3b, *ct*eIF3b WD40 domain and dissolved crystals, reflecting that the crystallized fragment only contains the WD40 domain of eIF3b.

Figure S2, related to Figure 2, showing the multiple sequence alignment of eIF3b orthologs.

Figure S3, related to Figure 2, displaying the electrostatic potential of conserved surface areas of cteIF3b-WD40.

Figure S4, related to Figure 3, showing the interaction studies between the eIF3b,i,g subcomplex and eIF3c using analytical SEC. No eIF3b,i,g,c complex was observed.

Figure S5, related to Figure 4, comparing the best fit of eIF3b-WD40 (blue) and eIF3i (yellow, PDB code: 3ZWL)

Figure S6, related to Figure 4, showing an eIF3b truncation (eIF3b$^{167\text{-}670}$) is able to bind to the 40S, but eIF3b$^{167\text{-}670}$, eIF3b$^{167\text{-}704}$-3i complex, eIF3i, eIF3g cannot interact with rpS9e.

Supplemental Experimental Procedures

Supplemental References

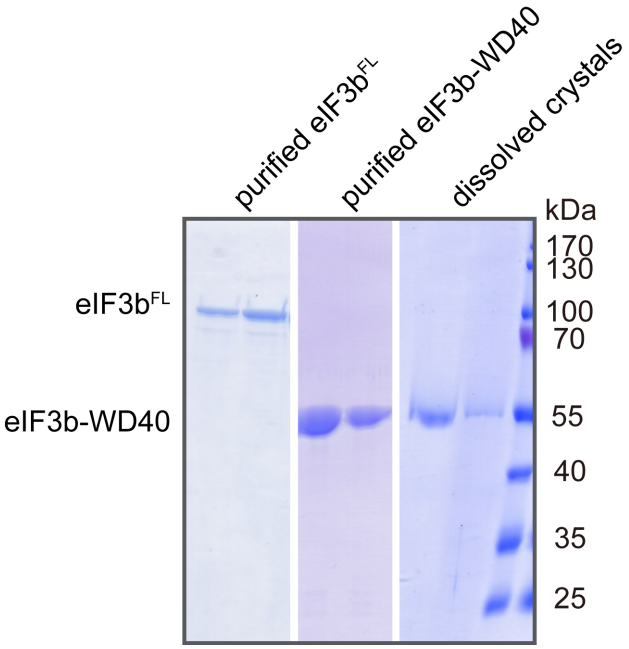

Figure S1, related to Figure 1. SDS-PAGE of full-length *cte*IF3b, *cte*IF3b WD40 domain and dissolved crystals.

The molecular weight of full-length *cte*IF3b and its WD40 domain are ~90 kDa and ~55 kDa, respectively. The size of the crystallized fragment is the same as *cte*IF3b WD40 domain.

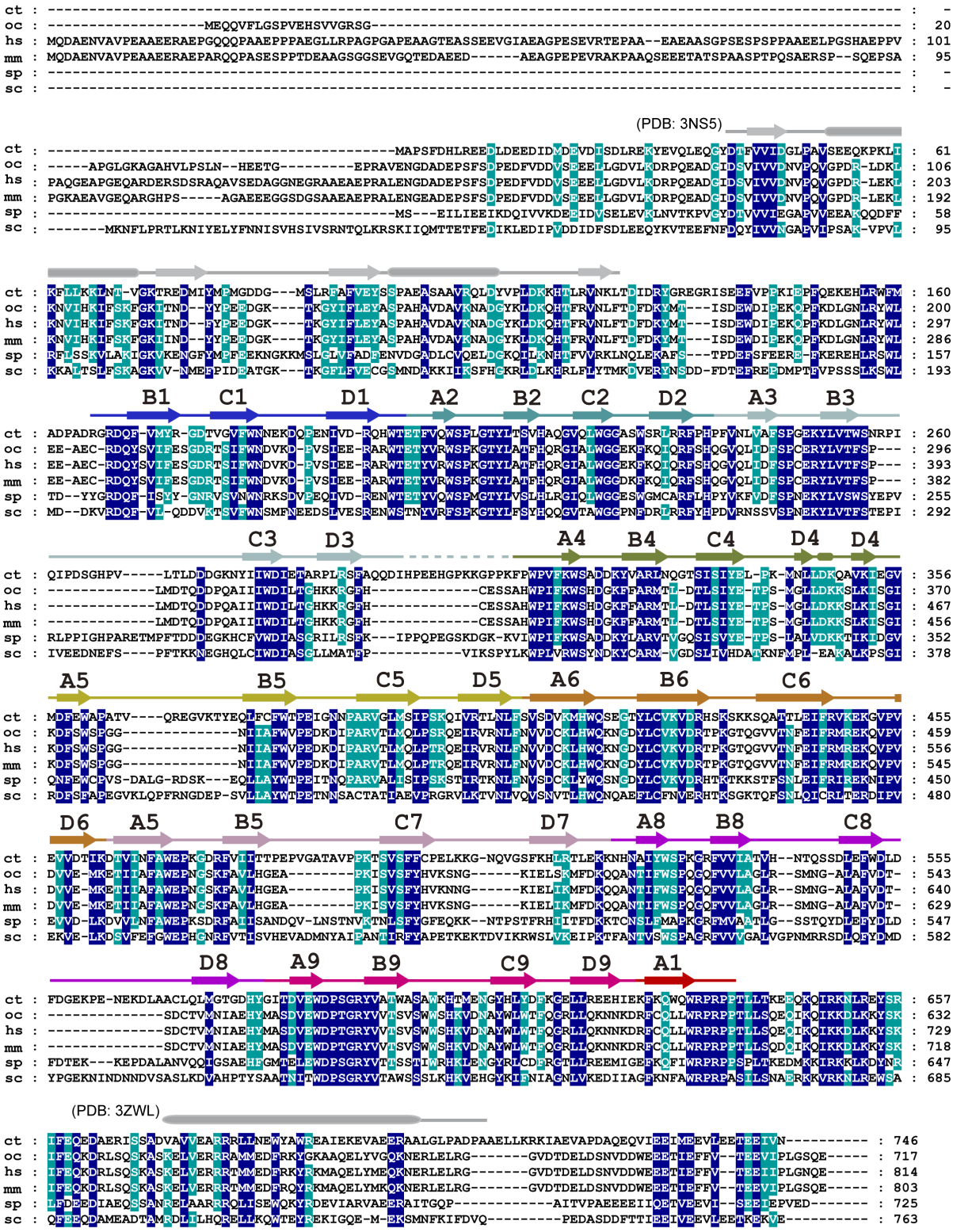

Figure S2, related to Figure 2. Multiple sequence alignment of eIF3b orthologs.

Amino acid sequences of eIF3b from *Chaetomium thermophilum* (ct), *Oryctolagus cuniculus*

(oc), *Homo sapiens* (hs), *Mus musculus* (mm), *Schizosaccharomyces pombe* (sp), and *Saccharomyces cerevisiae* (sc) are aligned using ClustalW2 (www.ebi.ac.uk/Tools/msa/clustalw2/, (Chenna et al., 2003)). Identical residues are highlighted with *blue* background and conserved residues with *cyan* background. Secondary structural elements (β-strands: arrows; α-helices: rounded rectangles; loops: lines) are indicated above the alignment (residues that were not built in the structure are represented as dashed lines). The WD40 domain of eIF3b is colored as in Fig 1B, while the N-terminal RRM domain and the C-terminal α-helix, which are not present in our structure, are colored light gray.

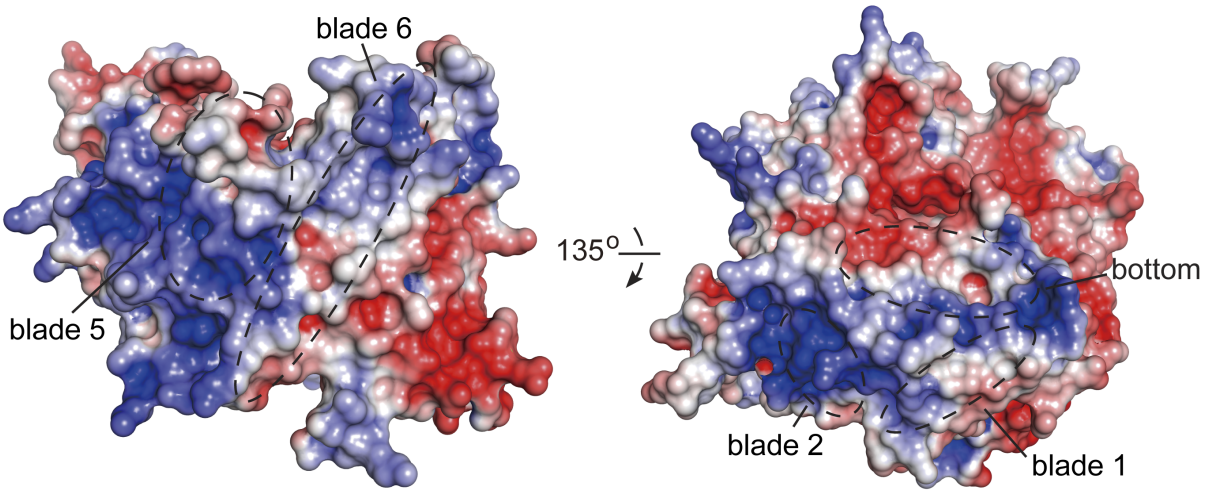

Figure S3, related to Figure 3. Electrostatic potential of conserved surface areas of *cte*IF3b-WD40.

The electrostatic surface potential of *cte*IF3b-WD40 colored from red (-5kT/e) through white (0kT/e) to blue (+5kT/e). Areas containing conserved surface residues are encircled and labeled based on blade numbers or propeller side. The orientations are similar to Fig 2C.

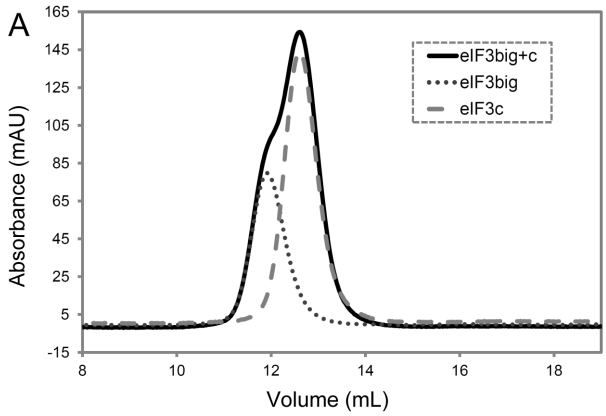

Figure S4, related to Figure 3. Interaction studies between the *ct*eIF3b,i,g subcomplex and *ct*eIF3c using analytical SEC.

Overlay of the analytical SEC profiles of the *ct*eIF3b-i-g subcomplex (dotted *black)*, *ct*eIF3c (dashed *gray*) and the *ct*eIF3b-i-g subcomplex together with subunit c (solid *dark*). In case of *ct*eIF3b,i,g + *ct*eIF3c, two overlapping peaks are observed; the main peak at a higher elution volume corresponds to eIF3c alone, whereas the smaller peak at a lower elution volume (forming the shoulder of the eIF3c peak) corresponds to the *ct*eIF3b,i,g complex. A shift to a lower elution volume does not occur, indicating that the *ct*eIF3b,i,g,c complex is not formed.

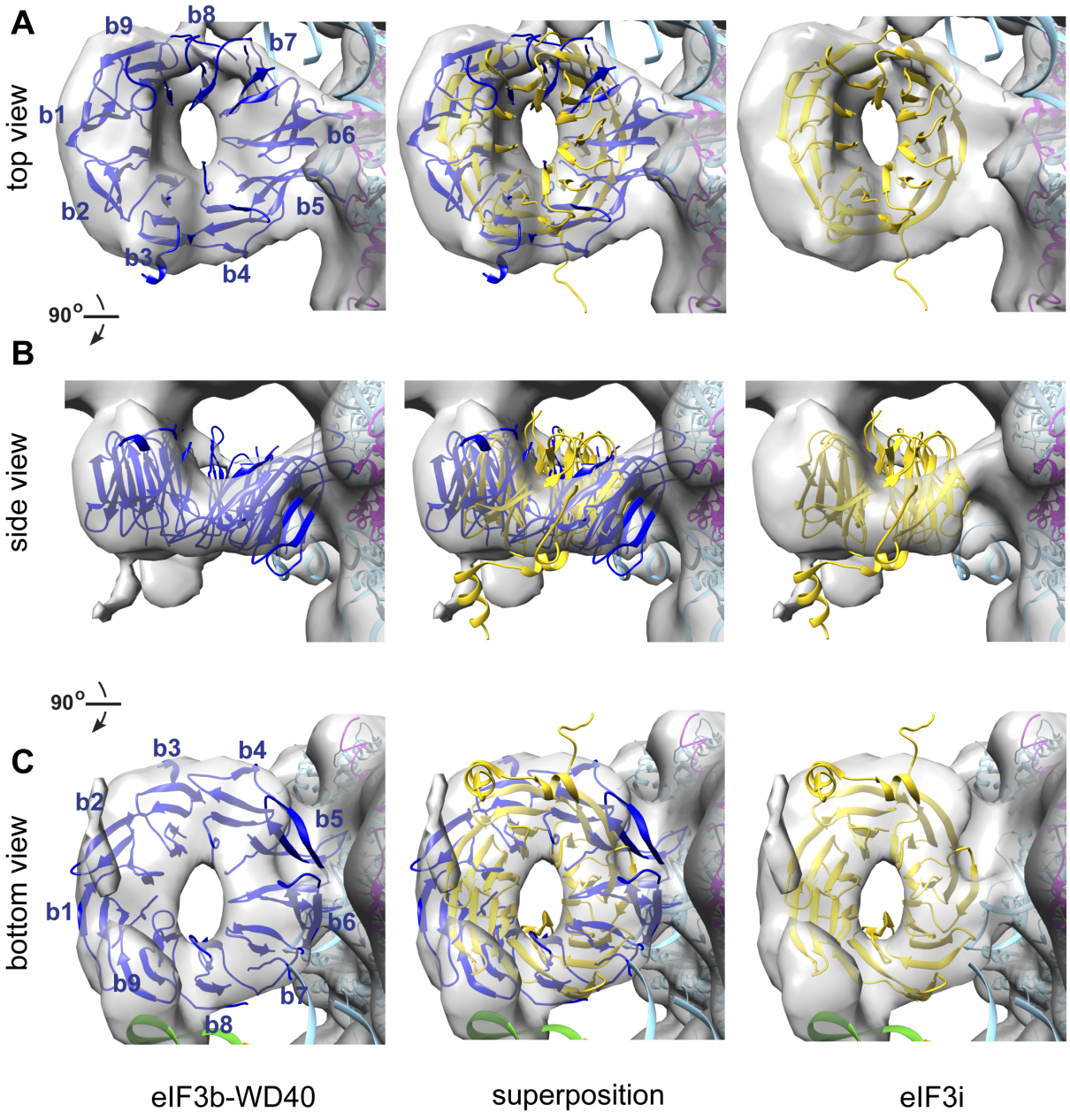

Figure S5, related to Figure 4. Comparison of the best fit of eIF3b-WD40 (blue) and eIF3i (yellow, PDB code: 3ZWL) into the density map of rabbit 43S initiation complex (grey, EMDB ID: 5658). In figure 5A the density assigned to DHX29 located above the doughnut-like density was removed for clarity.

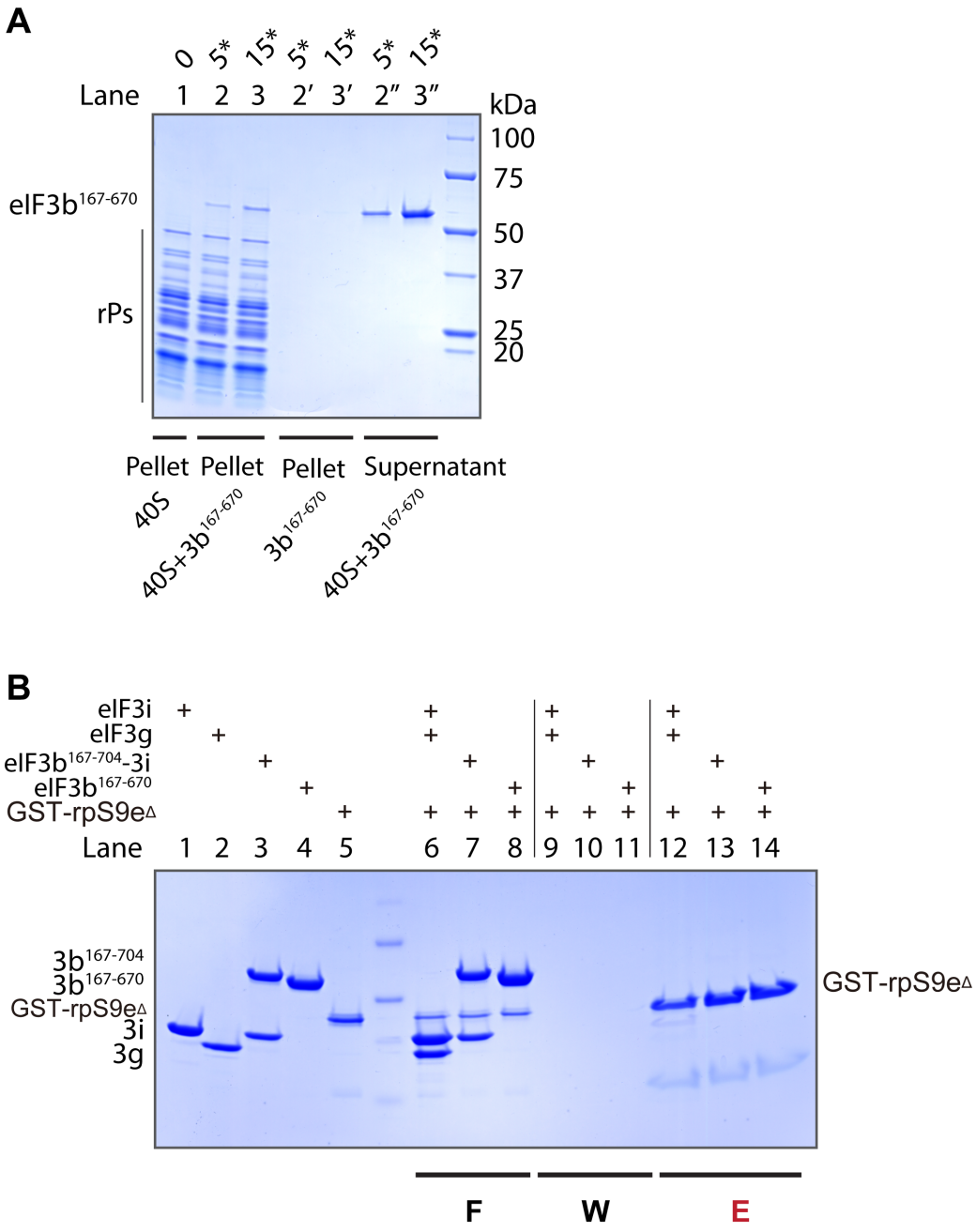

Figure S6, related to Figure 4. Interaction assays between eIF3b truncations and the 40S as well as rpS9e

(**A**) Co-sedimentation of eIF3b$^{167-670}$ and 40S ribosomes. eIF3b$^{167-670}$ co-sediments with 40S (Lanes 2-3) and excess eIF3b$^{167-670}$ remains in the supernatant (Lanes 2"-3"). Lane 1 and Lanes 2'-3' show controls of 40S alone and protein, respectively. (**B**) Interaction study between eIF3b truncations, eIF3i, eIF3g and rpS9e by GST pull-down assays. Lanes 1-5 show

the single proteins as reference. Lanes 12-14 show the elution fractions of the GST pull-down after the removal of unbound proteins (Lanes 6-8) and extensive washing (Lanes 9-11). rpS9e$^{\Delta}$ corresponds to rpS9e$^{1\text{-}183}$. No binding of eIF3b$^{167\text{-}670}$ or eIF3b$^{167\text{-}704}$-eIF3i complex to rpS9e can be detected. A wear binding between eIF3i and eIF3g complex and rpS9e could be detected (lane 12).

Supplemental Experimental Procedures

Cloning, protein expression and purification

Genes encoding eIF3b, a, c, i, and g were amplified by PCR from *Chaetomium thermophilum* genomic DNA, and the *ct*rpS9e gene from cDNA. Each gene was cloned into the pGEX-6P-1 vector (GE Healthcare), with the exception of eIF3a, which was cloned into the pET-28b vector (Merck), following the In-Fusion HD cloning kit user manual (Clontech). The ORFs of eIF3b$^{167\text{-}670}$ and eIF3b$^{167\text{-}704}$ were subcloned into the pGEX-6P-1 vector (GE Healthcare), while eIF3b$^{167\text{-}C}$ into a modified pETDuet-1 vector. The GST fusion proteins (containing a Prescission protease cleavage site), eIF3a with C-terminal His_6-tag and eIF3b$^{167\text{-}C}$ with N-terminal His_6-tag were individually expressed in *Escherichia coli* strain BL21 (DE3) grown in 2×YT medium. Target protein expression was induced by addition of isopropyl β-D-thiogalactopyranoside (IPTG) to a final concentration of 0.25 mM at an OD_{600} of ~1.0. Cells were harvested after incubation overnight at 16 °C by centrifugation (4,800 xg, 20 min, 4 °C; Beckman) and resuspended in lysis buffer (25 mM HEPES/NaOH, pH 7.5, 500 mM NaCl, 5% glycerol and 5 mM β-mercaptoethanol (β-ME)). A microfluidizer (Microfluidics, Newton, US) was used to rupture the bacterial cells and the cell debris was separated via centrifugation (30,000 xg, 35 min, 4 °C). For the GST fusion proteins the supernatant was applied to a GSTrap column (GE Healthcare) equilibrated in lysis buffer. After sample loading and extensive washing with lysis buffer, the column was equilibrated in a low salt buffer (25 mM HEPES/NaOH, pH 7.5, 100 mM NaCl, 5% glycerol and 5 mM β-ME). The GST fusion proteins were eluted with the low salt buffer containing additional 30

mM reduced glutathione. The GST-tag was cleaved by Prescission protease at 4 °C overnight at a 1:100 mass ratio of protease to fusion protein.

For further purification of full-length eIF3b and eIF3g, respectively, the protein was loaded onto an ion exchange column (GE healthcare) (Source 30Q for eIF3b; SP sepharose for eIF3g) equilibrated in buffer A (25 mM HEPES/NaOH, pH 7.5, 100 mM NaCl, 5% glycerol and 5 mM β-ME) and the target protein was eluted applying a linear gradient to buffer B (25 mM HEPES/NaOH, pH 7.5, 1 M NaCl, 5% glycerol and 5 mM β-ME).

For the eIF3a-His_6 protein the supernatant after cell rupture and centrifugation was applied to an IMAC column (His60 Ni superflow, Clontech). After sample loading and extensive washing with lysis buffer, the column was equilibrated in a low salt buffer (25 mM HEPES/NaOH, pH 7.5, 200 mM NaCl, 5% glycerol and 5 mM β-ME). eIF3a-His_6 was eluted with the low salt buffer containing additional 400 mM imidazole. Subsequently eIF3a-His_6 was loaded onto a HiTrap Heparin HP column (GE healthcare) equilibrated in buffer A (20 mM HEPES/NaOH, pH 7.3, 200 mM NaCl, 5% glycerol and 5 mM β-ME) and was eluted with a linear gradient to buffer B (20 mM HEPES/NaOH, pH 7.5, 1 M NaCl, 10% glycerol and 5 mM β-ME).

Final purification of the proteins (eIF3b, eIF3b$^{167\text{-}670}$, eIF3b$^{167\text{-}C}$, c, i, g, rpS9e and eIF3b$^{167\text{-}704}$-eIF3i complex as well as eIF3a-b-c complex) was achieved by a Superdex 200 (26/60) gel filtration column (GE Healthcare) in 10 mM HEPES/NaOH, pH 7.5, 150 mM NaCl, 2% glycerol and 2 mM DTT. Protein-containing fractions were pooled, concentrated, flash-frozen in liquid nitrogen and stored at -80 °C.

The selenomethionine (SeMet) substituted *ct*eIF3b was expressed in the methionine auxotroph *E. coli* strain B834 (DE3). The cells were initially grown in M9 mineral medium supplied with 50 $mg \cdot L^{-1}$ methionine until an OD_{600} of ~0.6 was reached. The medium was then removed by centrifugation (2,500 xg, 15 min, 4 °C) and the cells were resuspended in new M9 medium, which was supplemented with 50 $mg \cdot L^{-1}$ selenomethionine after residual methionine was depleted. Target protein expression was induced by addition of IPTG to a final concentration of 0.25 mM. The purification of selenomethionine labeled *ct*eIF3b was analogous to the wild type protein purification.

Crystallization and X-ray data collection

Initial crystallization screening for full-length *ct*eIF3b (12 $mg \cdot ml^{-1}$) was performed using the sitting drop vapor diffusion method with droplet compositions of 0.25µl : 0.25µl or 0.25µl : 0.125µl for protein and reservoir solutions, respectively. In total, 1056 commercially available conditions at 4 °C and 20 °C have been tested. Bipyramidal crystals were obtained at 20 °C from both droplets from JBScreen Nuc-Pro HTS (Jena Bioscience) with 15% (w/v) PEG 20k, 0.08 M $MnCl_2$, 0.1 M MES, pH 6.5 after approximately 30 days. Crystals of SeMet derivative protein were grown under the same conditions. Prior to X-ray data collection, crystals were transferred into the cryoprotectant buffer (crystallization condition supplemented with 23% (v/v) of ethylene glycol) for 5 seconds and then plunged into liquid nitrogen. A native diffraction dataset was collected from a single crystal at 100K at beamline P13 at PETRA III, DESY (Hamburg, Germany), while the MAD datasets of Se-Met substituted protein crystals were collected at wavelengths of 0.9798 Å (peak), 0.9799 Å

(inflection) and 0.9775 Å (remote) at beamline 14.1, BESSY II (Berlin, Germany, (Mueller et al., 2012)).

Structure determination and refinement

Data were processed and scaled using the programs XDS and XSCALE (Kabsch, 2010a, b) to a final resolution of 2.72 Å and 3.30 Å for native and Se-Met derivative *ct*eIF3b, respectively. Using the Se-MAD peak, inflection and remote diffraction datasets, six (out of seven expected) selenium atoms were found using the program SHELXD (Sheldrick, 2008) and initial phases were calculated at 4 Å resolution. Se positions were further refined using SHARP (Vonrhein et al., 2007) followed by density modification using the program Solomon (Abrahams and Leslie, 1996). An initial poly-alanine model was built by ARP/wARP (Langer et al., 2008) and refined against Se-Met data with Refmac5 (Morris et al., 2004; Perrakis et al., 1999), which was used for manual rebuilding and sequence assignment in Coot (Emsley et al., 2010). Due to the lack of isomorphism between Se-Met and native crystals (the c axis differs in length by 14.7 Å, see Supplementary Table S1), this initial model of the *ct*eIF3b WD40 domain was positioned by molecular replacement into the unit cell of the native crystal. Further model optimization and completion has been performed against the native data. Prior to structural refinement, randomly selected 5% test set of the reflections were set aside for the calculation of R_{free} as a quality monitor (Brunger, 1992, 1993). Refinement was performed with the PHENIX package (Adams et al., 2010). The electrostatic surface potential was calculated with PDB2PQR (Dolinsky et al., 2007) and displayed using the APBS plugin of the PyMol software.

Analytical size exclusion chromatography

An analytical Superdex 200 (10/300) column (GE healthcare) was used for the *in vitro* reconsititution of eIF3 subcomplexes. The buffer contained 25 mM HEPES/NaOH, pH 7.5, 150 mM NaCl, 5% glycerol and 2.5 mM β-ME. In each case, ~50 µg protein in a volume of 400 µl was injected on the column at a flow rate of 0.5 ml·min^{-1}.

GST pull-down assays

50 µg GST fusion protein was mixed with two-fold molar excess of non-tagged protein in a buffer containing 25 mM HEPES/NaOH, pH 7.5, 100 mM NaCl, 5% glycerol and 2.5 mM β-ME and incubated for 30 min with 100 µl glutathione beads. After washing four times with 1 mL buffer, bound protein was eluted with the same buffer containing additional 30 mM reduced glutathione.

Supplemental References

Abrahams, J.P., and Leslie, A.G. (1996). Methods used in the structure determination of bovine mitochondrial F1 ATPase. Acta Crystallogr. D *52*, 30-42.

Adams, P.D., Afonine, P.V., Bunkoczi, G., Chen, V.B., Davis, I.W., Echols, N., Headd, J.J., Hung, L.W., Kapral, G.J., Grosse-Kunstleve, R.W.*, et al.* (2010). PHENIX: a comprehensive Python-based system for macromolecular structure solution. Acta Crystallogr D Biol Crystallogr *66*, 213-221.

Brunger, A.T. (1992). Free R value: a novel statistical quantity for assessing the accuracy of crystal structures. Nature *355*, 472-475.

Brunger, A.T. (1993). Assessment of phase accuracy by cross validation: the free R value. Methods and applications. Acta Crystallogr D Biol Crystallogr *49*, 24-36.

Chenna, R., Sugawara, H., Koike, T., Lopez, R., Gibson, T.J., Higgins, D.G., and Thompson, J.D. (2003). Multiple sequence alignment with the Clustal series of programs. Nucleic Acids Res *31*, 3497-3500.

Dolinsky, T.J., Czodrowski, P., Li, H., Nielsen, J.E., Jensen, J.H., Klebe, G., and Baker, N.A. (2007). PDB2PQR: expanding and upgrading automated preparation of biomolecular structures for molecular simulations. Nucleic Acids Res. *35*, W522-525.

Emsley, P., Lohkamp, B., Scott, W.G., and Cowtan, K. (2010). Features and development of Coot. Acta Crystallogr D Biol Crystallogr *66*, 486-501.

Kabsch, W. (2010a). Integration, scaling, space-group assignment and post-refinement. Acta Crystallogr D Biol Crystallogr *66*, 133-144.

Kabsch, W. (2010b). XDS. Acta Crystallogr D Biol Crystallogr *66*, 125-132.

Langer, G., Cohen, S.X., Lamzin, V.S., and Perrakis, A. (2008). Automated macromolecular model building for X-ray crystallography using ARP/wARP version 7. Nat Protoc *3*, 1171-1179.

Morris, R.J., Zwart, P.H., Cohen, S., Fernandez, F.J., Kakaris, M., Kirillova, O., Vonrhein, C., Perrakis, A., and Lamzin, V.S. (2004). Breaking good resolutions with ARP/wARP. J Synchrotron Radiat *11*, 56-59.

Mueller, U., Darowski, N., Fuchs, M.R., Forster, R., Hellmig, M., Paithankar, K.S., Puhringer, S., Steffien, M., Zocher, G., and Weiss, M.S. (2012). Facilities for macromolecular crystallography at the Helmholtz-Zentrum Berlin. J Synchrotron Radiat *19*, 442-449.

Perrakis, A., Morris, R., and Lamzin, V.S. (1999). Automated protein model building combined with iterative structure refinement. Nat Struct Biol *6*, 458-463.

Sheldrick, G.M. (2008). A short history of SHELX. Acta Crystallogr A *64*, 112-122.

Vonrhein, C., Blanc, E., Roversi, P., and Bricogne, G. (2007). Automated structure solution with autoSHARP. Methods Mol. Biol. *364*, 215-230.